U.P.B. Sci. Bull., Series D, Vol. 85, Iss. 4, 2023 ISSN 1354-2358

NUMERICAL SIMULATION OF TURBULENT NATURAL CONVECTION IN LNG CYLINDRICAL TANK WITH EVAPORATION

M.S. KHELIFI -TOUHAMI[1]

This study quantitatively examines turbulent natural convection in a heated cylindrical tank filled with liquefied natural gas (LNG). It employs Reynolds-averaged Navier-Stokes (RANS) with a low Reynolds number k-epsilon model and considers evaporative cooling. The simulation accurately captures turbulence dynamics, making it a valuable tool for predicting fluid behavior in the tank. Results reveal the relationship between Rayleigh number, flow intensity, and temperature fluctuations. Higher Rayleigh numbers lead to increased turbulent flow and viscosity. Recirculation jets form at the base, with the highest viscosity. The study also identifies non-uniform evaporative heat flux, intensified by turbulence and higher Rayleigh numbers.

Keywords: LNG tank, Low Reynolds number, Lateral heating, evaporative heatflux

1. Introduction

Thermal engineering uses natural convection flows in cavities for a variety of things, including cooling electronics, solar collectors, home insulation, and fuel storage tanks. A wealth of experimental information on laminar and turbulent flows in square cavity configurations allows for useful comparisons with numerical simulations. For instance, Ampofo and Karayiannis [1] compared their numerical findings from Vasic and Hanjalic [2], Peng, and Davidson [3] with their experimental findings of turbulent flows in a square cavity that had been differentially heated. Additionally, to measure the evaporation of these liquids using the Schlieren method, Khemis et al. [4] and Boukeffa et al. [5] carried out experimental studies on natural convection in cryostats containing liquid nitrogen. Kanazawa et al. [6] performed an experimental visualization of the convective flow profile in an LNG tank heated from the bottom and sidewalls. In order to better understand natural convection in cryogenic tanks, numerical studies have been done. While Bates and Morrison [7], as well as Pham and Petit [8], numerically investigated the rollover phenomenon in turbulent flow in a square cavity containing LNG, Li et al. [9] investigated the effect of liquid level on heat transfer in a nitrogen storage tank. Hubert et al. [10] have done a recent numerical

---

[1] Dr., Department of Hydrocarbon Transport and Equipment, Laboratory of Hydrocarbon Physical Engineering, Faculty of Hydrocarbons and Chemistry (FHC), University of M'Hamed Bougara Boumerdes, 35000, Algeria, e-mail: s.khelifi@univ-boumerdes.dz

study of the dynamic behavior of LNG in a storage tank during the same phenomenon. When Roh et al. [11] numerically analyzed natural convection in an LNG storage tank; they discovered that the Boil off generation (BOG) is strongly dependent on the solid-liquid contact.

Chen et al. [12] conducted a similar analysis of temperature and pressure changes in an LNG storage tank. Haddar et al. [13] suggested installing a cooling system inside LNG tanks to absorb heat loss to the environment and lower the BOG rate. Finally yet importantly, Hasan et al. [14] showed that reducing BOG is influenced by various variables, including ambient temperature, LNG tank pressure, and LNG composition.

In numerical simulations of natural laminar convection in an LNG cylindrical cavity, Khelifi-Touhami et al. [15] discovered that evaporation is not uniform. Kozhevnikov and Sheremet [16] considered the dimensionless Marangoni term in their numerical calculations to examine the impact of surface tension on evaporation during natural LNG convection in the same configuration. Additionally, the study of Rachedi et al. [17] gave us more information on the Marangoni number-based evaporative heat flux. Based on the Rayleigh number, they showed how this parameter affects evaporation at the free surface. In this paper, we seek to investigate the effects of the Rayleigh number on the velocity, temperature, and turbulent viscosity fields, as well as pinpoint the tank's transitional region to turbulence.

2. Governing equations

Fig.1 illustrates the investigation's issue. The two-dimensional computational domain is housed in a cylindrical tank with a diameter of D and a height of H and an aspect ratio of Al equal to one. The tank's top is a free surface where evaporation takes place, and its base is assumed adiabatic. There is a constant heat flux against the sidewall. The cavity's size can be increased while maintaining a constant lateral heat flux by raising the Rayleigh number Ra above 10^8. When LNG is heated laterally, the fluid density changes, causing hotter liquid masses to rise along the wall of the cavity, cool, and then fall in the center. As long as the heating continues, the liquid will continuously recirculate. According to the Boussinesq approximation, the fluid flow is assumed incompressible, viscous, and turbulent. The time-averaged Navier-Stokes equations in cylindrical coordinates and the continuity equation serve as the governing equations using for example the work of Launder and Spalding [18]. The low Reynolds number k-epsilon model is adapted in this situation to simulate the Reynolds stresses with FLB model detailed in the research of Fan, Lakshminarayana and Barnett [19].

The following variables are added in Equation (1) to scale the following governing equations:

$$r = \frac{r^*}{H},\quad z = \frac{z^*}{H},\quad u = \frac{u^* H}{\nu},\quad \upsilon = \frac{\upsilon^* H}{\nu},\quad p = \frac{p^*}{\rho \upsilon^2},\quad T_m^* = \frac{T_i^* - T_0^*}{2}$$
$$T = \frac{T^* - T_m^*}{T_i^* - T_0^*},\quad k = \frac{H^2 k^*}{\nu^2},\quad \varepsilon = \frac{H^4 \varepsilon^*}{\nu^3},\quad \nu_t = \frac{\nu_t^*}{\nu} \tag{1}$$

Continuity equation

$$\frac{1}{r}\frac{\partial (ru)}{\partial r} + \frac{\partial \upsilon}{\partial z} = 0 \tag{2}$$

Momentum equations

$$\frac{\partial u}{\partial t} + \frac{1}{r}\frac{\partial (ruu)}{\partial r} + \frac{\partial (u\upsilon)}{\partial z} = -\frac{\partial p}{\partial r} + \frac{1}{r}\frac{\partial}{\partial r}\left[r(1+\nu_t)\frac{\partial u}{\partial r}\right] + \frac{\partial}{\partial z}\left[(1+\nu_t)\frac{\partial u}{\partial z}\right]$$
$$-(1+\nu_t)\frac{u}{r^2} + S_u \tag{3}$$

$$\frac{\partial \upsilon}{\partial t} + \frac{1}{r}\frac{\partial (r\upsilon u)}{\partial r} + \frac{\partial (\upsilon\upsilon)}{\partial z} = -\frac{\partial p}{\partial z} + \frac{1}{r}\frac{\partial}{\partial r}\left[r(1+\nu_t)\frac{\partial \upsilon}{\partial r}\right] + \frac{\partial}{\partial z}\left[(1+\nu_t)\frac{\partial \upsilon}{\partial z}\right]$$
$$- GrT + S_\upsilon \tag{4}$$

Energy equation

$$\frac{\partial T}{\partial t} + \frac{1}{r}\frac{\partial (ruT)}{\partial r} + \frac{\partial (\upsilon T)}{\partial z} = \frac{1}{r}\frac{\partial}{\partial r}\left[r\left(\frac{1}{\Pr} + \frac{\nu_t}{\sigma_t}\right)\frac{\partial T}{\partial r}\right] + \frac{\partial}{\partial z}\left[\left(\frac{1}{\Pr} + \frac{\nu_t}{\sigma_t}\right)\frac{\partial T}{\partial z}\right] \tag{5}$$

Turbulent equation for kinetic energy, k

$$\frac{\partial k}{\partial t} + \frac{1}{r}\frac{\partial (ruk)}{\partial r} + \frac{\partial (\upsilon k)}{\partial z} = \frac{1}{r}\frac{\partial}{\partial r}\left[r\left(1 + \frac{\nu_t}{\sigma_k}\right)\frac{\partial k}{\partial r}\right] + \frac{\partial}{\partial z}\left[\left(1 + \frac{\nu_t}{\sigma_k}\right)\frac{\partial k}{\partial z}\right] + S_k \tag{6}$$

The dissipation rate equation for kinetic energy, ε

$$\frac{\partial \varepsilon}{\partial t} + \frac{1}{r}\frac{\partial (ru\varepsilon)}{\partial r} + \frac{\partial (\upsilon \varepsilon)}{\partial z} = \frac{1}{r}\frac{\partial}{\partial r}\left[r\left(1 + \frac{\nu_t}{\sigma_\varepsilon}\right)\frac{\partial \varepsilon}{\partial r}\right] + \frac{\partial}{\partial z}\left[\left(1 + \frac{\nu_t}{\sigma_\varepsilon}\right)\frac{\partial \varepsilon}{\partial z}\right] + S_\varepsilon \tag{7}$$

The equations (8) give the sources terms of the k epsilon model.

$$\nu_t = C_\mu f_\mu \frac{k^2}{\varepsilon}$$

$$P_k = \nu_t\left[2\left(\frac{\partial u}{\partial r}\right)^2 + 2\left(\frac{u}{r^2}\right)^2 + \left(\frac{\partial u}{\partial z} + \frac{\partial \upsilon}{\partial r}\right)^2 + 2\left(\frac{\partial \upsilon}{\partial z}\right)^2\right]$$

$$S_u = \frac{\partial}{\partial z}\left[\nu_t \frac{\partial \upsilon}{\partial r}\right] + \frac{1}{r}\frac{\partial}{\partial r}\left[r\nu_t \frac{\partial u}{\partial r}\right] - \nu_t \frac{u}{r^2}$$

$$S_{\upsilon} = \frac{\partial}{\partial z}\left[\nu_t \frac{\partial \upsilon}{\partial z}\right] + \frac{1}{r}\frac{\partial}{\partial r}\left[r\nu_t \frac{\partial u}{\partial z}\right]$$

$$S_k = P_k - \varepsilon - Gr\left[\frac{\nu_t}{\sigma_t}\frac{\partial T}{\partial z}\right] + D$$

$$S_{\varepsilon} = \frac{\varepsilon}{k}\left[f_1 C_{1\varepsilon} P_k - C_{3\varepsilon} Gr \frac{\partial T}{\partial z} - f_2 C_{2\varepsilon}\varepsilon\right] + E$$

$$Gr = \frac{g\beta\left(T_i^* - T_0^*\right)H^3}{\nu^2}, \quad \Pr = \frac{\nu}{a}, \quad Ra = Gr\Pr$$

$$C_{\mu} = 0.09, \quad \sigma_t = 0.9, \quad \sigma_k = 1, \quad \sigma_{\varepsilon} = 1.3, \quad C_{1\varepsilon} = 1.44, \quad C_{2\varepsilon} = 1.92$$

$$C_{3\varepsilon} = \tanh\left|\frac{\upsilon}{u}\right| \tag{8}$$

The equations (9) give the damping functions of FLB model [19].

$$D = 0, \quad E = 0, \quad R_y = y_{\min}\sqrt{k}, \quad R_T = \frac{k^2}{\varepsilon}$$

$$f_1 = 1, \quad f_w = 1 - \exp\left[-\frac{\sqrt{R_y}}{2.3} + \left(\frac{\sqrt{R_y}}{2.3} - \frac{R_y}{8.89}\right)\left(1 - \exp\left(\frac{R_y}{20}\right)\right)^3\right]$$

$$f_2 = \left[1 - 0.22\exp\left(-\frac{R_T^2}{36}\right)\right] f_w^2, \quad f_{\mu} = \frac{0.4 f_w}{\sqrt{R_T}} + \left[1 - 0.4\frac{f_w}{R_T}\right]\left[1 - \exp\left(-\frac{R_y}{42.63}\right)\right]^3 \tag{9}$$

Fan et al. [19] state that Eq. (9) is in terms of Ry and that the previous formula can handle unsteady flow since Ry was used in place of y+. Near the wall, the function fw is O(y). The effects of wall damping are taken into consideration in the current model by using fw as a near-wall function.

The numerical simulation in two dimensions will be limited to the calculation of the right half of the tank since the flow is assumed axisymmetric.

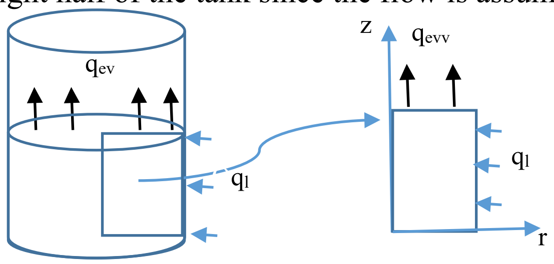

Fig.1 Graph of the physical model and the numerical domain

Boundary conditions

On the solid walls are given as follows:

$$u = \upsilon = k = 0, \quad \varepsilon = \frac{C_\mu^{3/4} k^{3/2}}{0.41 y_1} \tag{10}$$

y_1 : is the distance from the first node of the mesh to the wall

Note that the FLB model imposes a zero gradient boundary condition. However, we have decided to use a wall function condition in this work due to the observed numerical stability.

On the vertical wall:

$$\frac{\partial T}{\partial r} = 1 \tag{11}$$

On the horizontal wall:

$$\frac{\partial T}{\partial z} = 0 \tag{12}$$

On the axis:

$$u = 0, \quad \frac{\partial T}{\partial r} = \frac{\partial \upsilon}{\partial r} = \frac{\partial k}{\partial r} = \frac{\partial \varepsilon}{\partial r} = 0 \tag{13}$$

On the free surface of the liquid:

$$\upsilon = 0, \quad \frac{\partial T}{\partial z} = -\frac{q_{ev}^*}{q_l^*}, \quad \frac{\partial u}{\partial z} = \frac{\partial k}{\partial z} = \frac{\partial \varepsilon}{\partial z} = 0 \tag{14}$$

Pham and Petit [8], Khelifi-Touhami et al. [15], Hubert et al. [10], Kozhevnikov and Sheremet [16], and Rachedi et al. [17] all used the evaporation model proposed by Hashemi and Wesson [20] for precise modeling of LNG evaporation at the surface. This model employs the following dimensional conditions, given by Eq. (15), at the free surface:

$$\begin{aligned} &If \quad T^*(r^*,H) \succ T^*_{sat} \quad then \quad q^*_{ev} = c\lambda \left[\frac{g\beta}{a\nu}\right]^{1/3} \left[T^*(r^*,H) - T^*_{sat}\right]^{4/3} \quad with\; c = 0.13 \\ &If \quad T^*(r^*,H) \le T^*_{sat} \quad then \quad q^*_{ev} = 0 \end{aligned} \tag{15}$$

For the non-dimensional conditions Eq. (16) as written by [15] as follows:

$$\begin{aligned} &If \quad T(r,1) \succ 0 \quad then \quad q_{ev} = cRa^{1/3}\left[T(r,1) - 0\right]^{4/3} \quad with\; c = 0.13 \\ &If \quad T(r,1) \le 0 \quad then \quad q_{ev} = 0 \end{aligned} \tag{16}$$

3. Numerical methods

The governing equations are addressed through the application of the finite volume method. Specifically, the equations are integrated into a straightforward control volume that envelops each mesh node. Node positions are determined through the utilization of a hyperbolic tangent function or a geometric sequence to generate the mesh, enabling a denser refinement in proximity to the walls using the following equation (17) to generate the grid for example in square cavity as shown in fig.2.

$$\begin{cases} x1 = 2(i-1)/(m2-1) \\ xr(i) = 0.5\left[1+\dfrac{\tanh(2(x1-1))}{\tanh(2)}\right] \end{cases} \quad 2 \le i \le m2+1$$
$$\begin{cases} z1 = 2(j-1)/(n2-1) \\ xz(j) = 0.5\left[1+\dfrac{\tanh(2(z1-1))}{\tanh(2)}\right] \end{cases} \quad 2 \le j \le n2+1 \qquad (17)$$

Scalar variables are computed at the central nodes, while velocity components are computed in a staggered manner. The Semi-Implicit Method for Pressure Linked Equations Revised (SIMPLER) [21] is employed to correct pressure and velocity, ensuring adherence to the continuity equation. An entirely implicit approach is adopted to resolve the problem, with the triangular matrices generated by the discretization of the equations being solved using the Thomas algorithm. Subsequently, a comparative analysis of our results against experimental benchmarks is presented to validate our computations within the square cavity. Following this, a series of graphical representations is provided to illustrate the velocity and temperature fields for different Rayleigh values within a cylindrical LNG tank possessing a fixed aspect ratio of one.

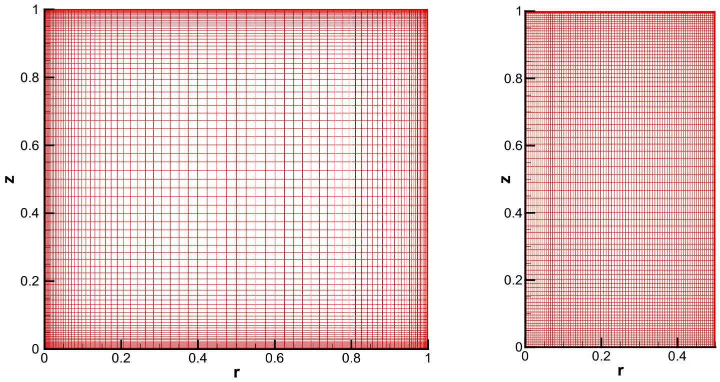

Fig.2 Grid used in the square cavity and in the cylindrical tank

3. 1. Validation in the square cavity

In light of the complete absence of experimental results in cylindrical coordinates, especially in the context of turbulent scenarios, the initial step involves the presentation of validation results obtained by in house FORTRAN program using Compaq Visual Fortran software [22] within a square cavity. For this study, the data provided by Ampofo and Karayiannis [1] were employed to facilitate the validation of numerical models. Prior to the presentation of Nusselt number variations on the hot and cold cavity sides and the assessment of turbulent kinetic energy variations in the cavity's central region relative to experimental data, a comprehensive examination of the program's mesh sensitivity was carried out.

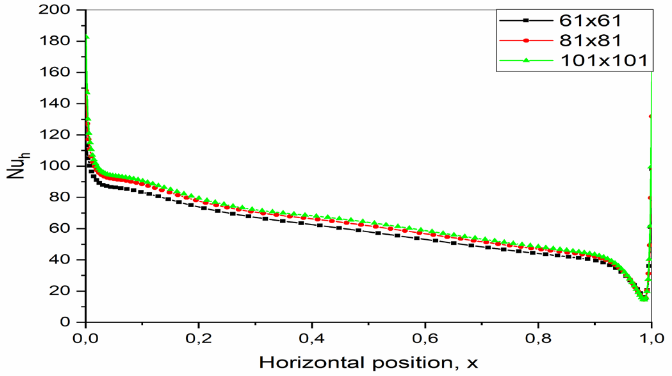

Fig.3 Nusselt number near the hot wall for various grids

In Fig.3, a series of numerical simulations were conducted with various mesh sizes to assess the sensitivity of the outcomes to node count. The chosen mesh size for subsequent simulations was based on the observation that results became nearly indistinguishable beyond an 81x81 configuration, facilitating comparisons with existing literature. A contrast was specifically drawn between the findings and experimental benchmark results presented by [1].

Fig.4.1 illustrates the results of simulations for the Nusselt number, indicating a decrease in the Nusselt number as the flow approaches the hot wall of the cavity, while it increases as the flow moves towards the cold wall.

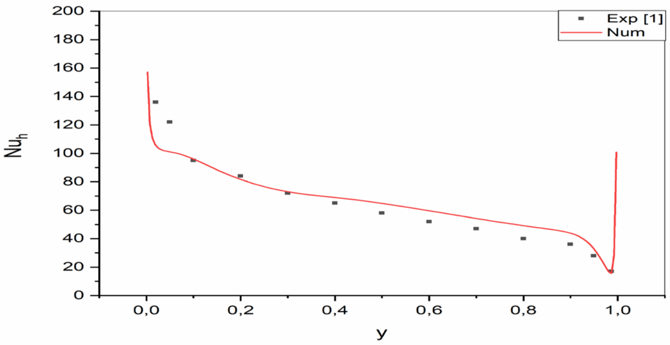

Fig.4.1 Nusselt number variation near the hot wall

It was observed that the Nusselt number obtained through simulation closely approximated the experimental results of [1] for both walls. However, a minor discrepancy in values was noted between y = 0.5 and 0.9 in Fig.4.2, where the maximum value reached 160, as opposed to the experimental value of 140, which was attained at the base of the hot wall and the top of the cold wall. This discrepancy is likely attributable to the higher refinement level in the numerical case.

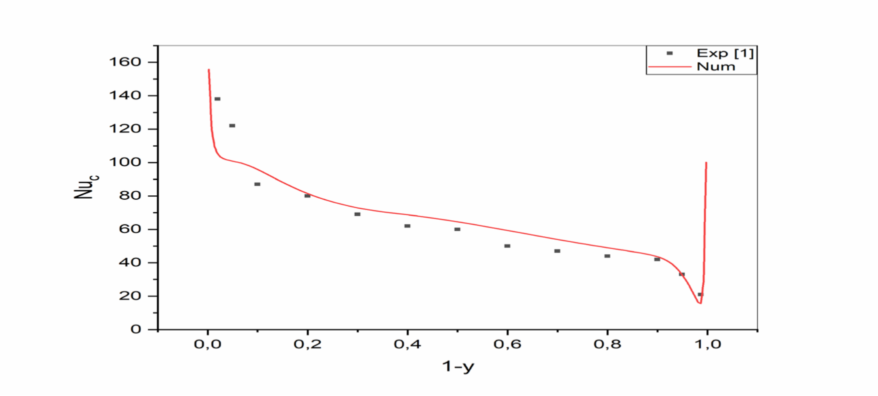

Fig.4.2 Nusselt number variation near the cold wall

In contrast to the previous numerical results for this case, the turbulent kinetic energy variation depicted in Fig.5 closely aligns with the experimental findings. The curve exhibits a maximum value of approximately 4.5, which closely matches the experimental data. It is worth noting that the standard k-epsilon model deviates from the experimental results by generating excessively high values near the wall. To achieve numerical results that closely resemble the actual behavior of the LNG storage tank, it is imperative to identify the most suitable turbulence model in order to obtain acceptable numerical results.

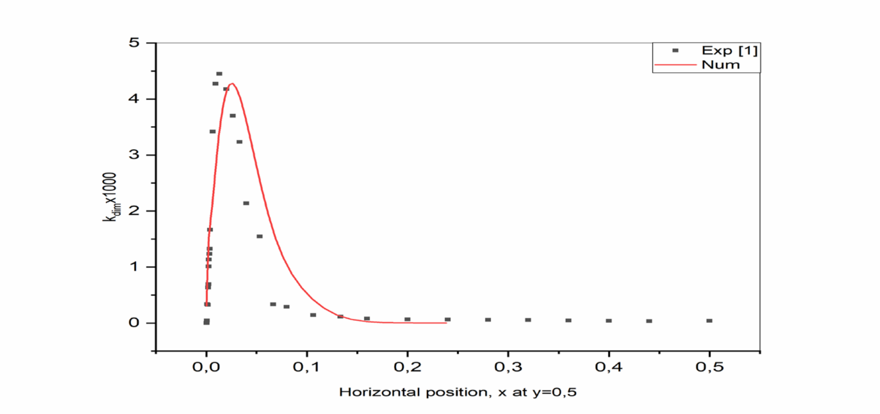

Fig.5 Dimensional kinetic energy variation at mid-height of the cavity y=0.5

3.2 Mesh sensitivity in the LNG tank

To determine how sensitive the numerical solutions are to changes in the number of nodes and mesh refinement around obstacles, a mesh sensitivity analysis must be carried out prior to beginning the modeling process. Fig.6 demonstrates that the axial velocity changes for various Rayleigh numbers are insignificant. As a result, the domain is simulated for all variables using an 81x81 grid.

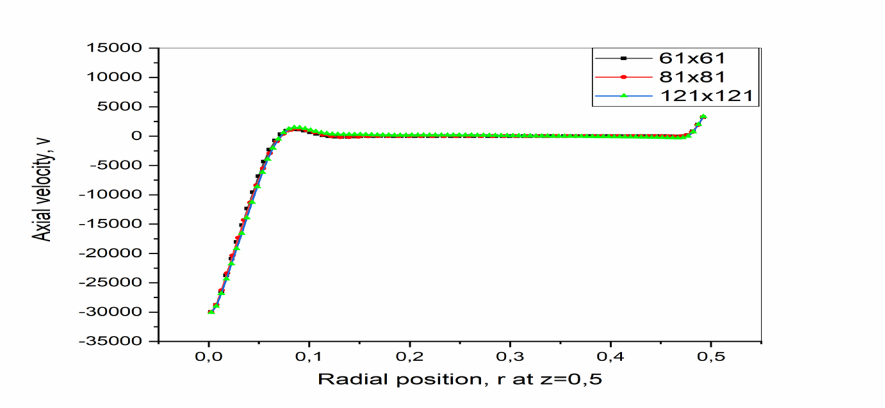

Fig.6 Mesh sensitivity for axial velocity at Ra=10^{11}

4. Results in the LNG tank

In this work, the average characteristics are presented, particularly the radial and axial velocity, as well as the dynamic and thermal fields on the vertical plane under study. Fig.7.1 and 7.2 show how the radial velocity varies along the vertical z-axis by fixing the radial position at r = 0.25 with respect to the axis. The fact that the values of the radial velocities are negative at the free surface and positive at the base of the tank serves as confirmation of the direction of fluid recirculation. Controlling the vertical fluctuation of the second velocity component is essential to ensuring that the fluid circulates in a loop.

Additionally, with the Rayleigh numbers taken into account, the velocities between 0.2 and 0.8 are nearly null, showing that the liquid does not move very much in this range. The velocity modules almost double when Ra goes from 10^8 to 10^9 or from 10^{10} to 10^{11}, whichever is at the top or bottom of the tank. As a result, the fluid's velocity rises as the Rayleigh number rises, and this impact is amplified as the Rayleigh number rises. As the temperature differential between the hot walls and the free surface rises, the floatability forces also rise.

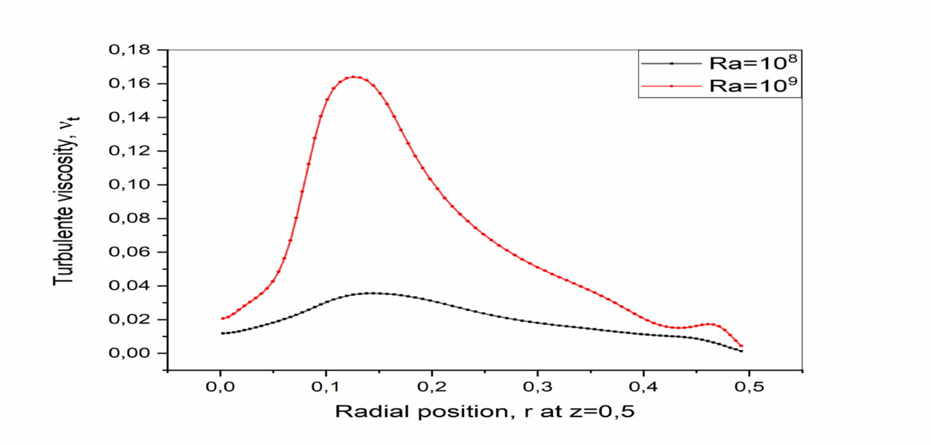

Fig.7.1 Turbulent viscosity variation at mid-height of the tank for Ra=10^8 and Ra=10^9

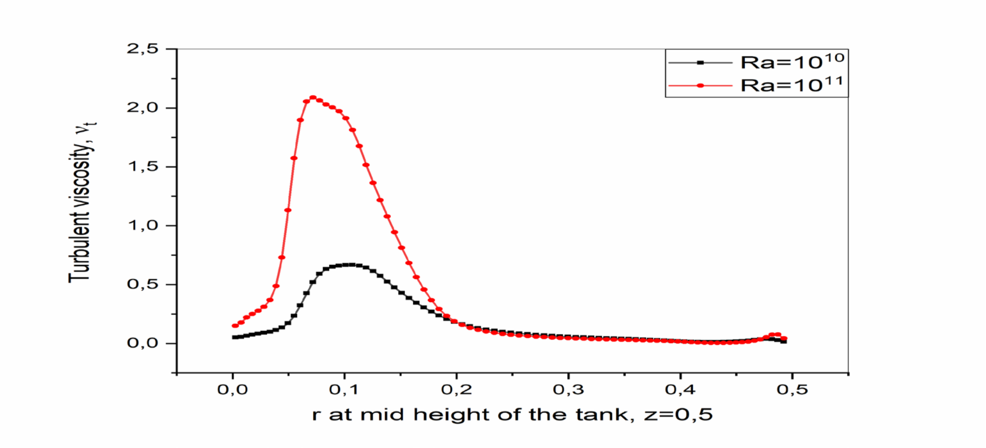

Fig.7.2 Turbulent viscosity variation at mid-height of the tank for Ra=10^{10} and Ra=10^{11}

The Rayleigh number is used to plot the variations in axial velocity at the tank's mid-height in Fig.8.1 and 8.2. The axial velocity at the axis of the tank significantly increases as the Rayleigh number rises. This indicates that the fluid is moving more quickly in the tank's middle at higher Rayleigh numbers. The change in axial velocity is less noticeable near the hot wall than it is in the tank's center, though. This is because the evaporative cooling causes the free surface, where the LNG flows meet, to fall back down. Fig.8.1 and 8.2, taken together, show how the axial velocity varies with the Rayleigh number in the tank.

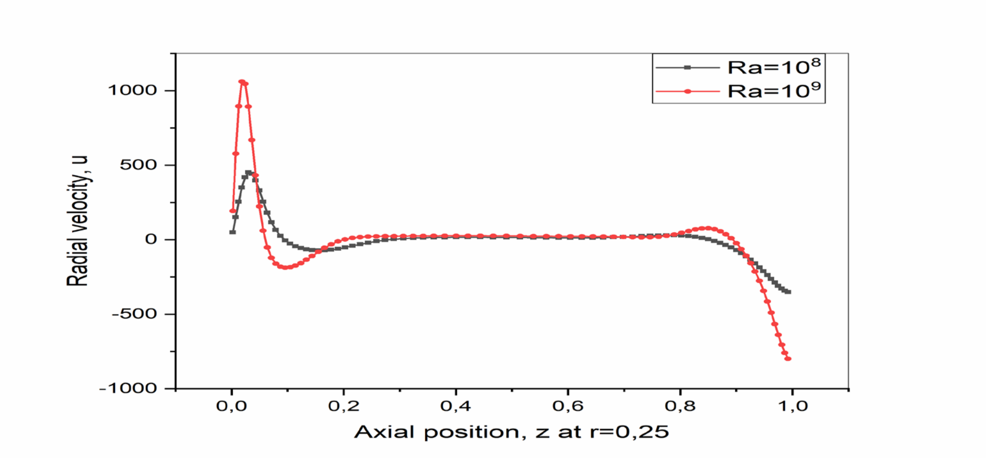

Fig.8.1 Radial velocity variation along the vertical position at r=0.25 for Ra=10^8 and Ra=10^9

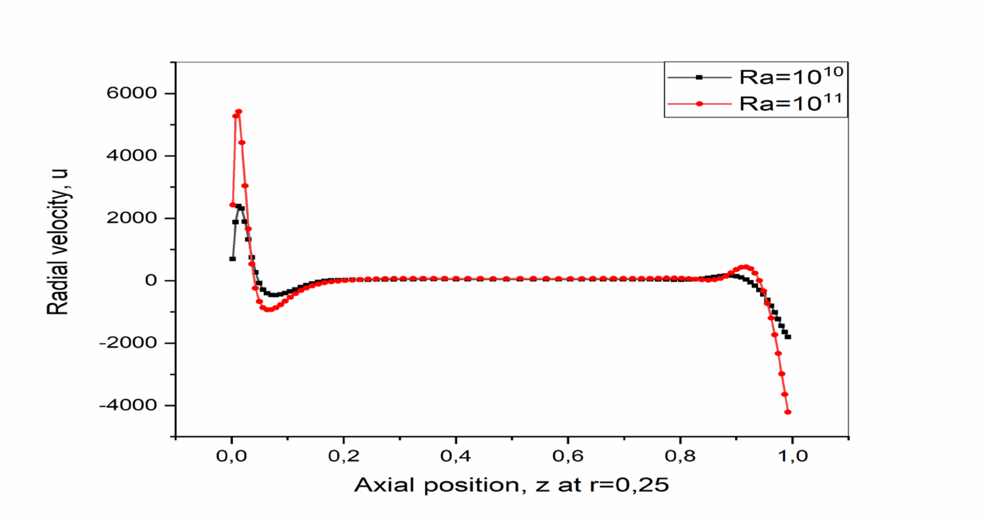

Fig.8.2 Radial velocity variation along the vertical position at r=0.25 for Ra=10^{10} and Ra=10^{11}

Fig.9.1 and 9.2 display the velocity and temperature fields for each Rayleigh number under consideration. The dimensionless temperature diminishes as the Rayleigh number increases. The fluid segregates into distinct layers based on temperature disparities, with the stratification of these layers, which become more pronounced. This behavior results from the velocity nearly reaching zero when the temperature is horizontally uniform for a given Rayleigh number. Furthermore, the velocity varies in the same direction as the Rayleigh number, intensifying the flow as Ra increases. It is important to note that, during laminar flow, the fluid circulates in a single loop within the tank, regardless of the aspect ratio.

As observed in Fig.9.1 and 9.2, a jet initiates from the central base after Ra = 10^8 and subsequently collides with the sidewall at Ra = 10^{10} and Ra = 10^{11}.

This collision gives rise to a secondary, smaller recirculation near the wall, rotating in the same direction as the primary recirculation and generating an upward flow towards the liquid surface. This presence of two recirculation zones signifies turbulent flow and higher Rayleigh numbers. These figures depict diverse flow patterns emerging at different Rayleigh numbers, providing a visual representation of the interplay between temperature, velocity, and Rayleigh number.

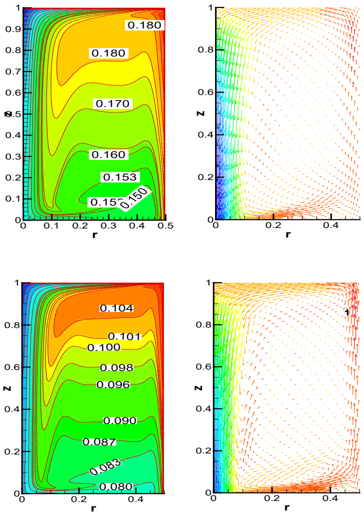

Fig.9.1 Velocity and temperature profiles for Ra=10^8 and Ra=10^9

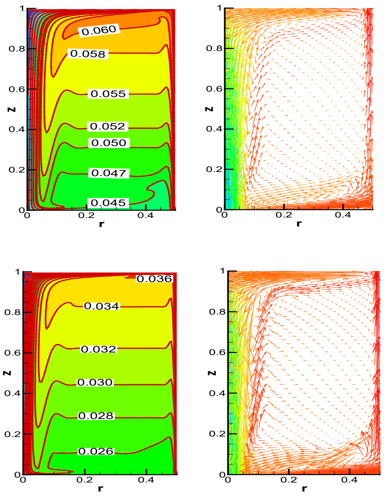

Fig.9.2 Velocity and temperature profiles for Ra=10^{10} and Ra=10^{10}

In this work's part, we examine how changing the Rayleigh number affects the turbulent viscosity at the reservoir's mid-height for different Rayleigh numbers (Figs.10.1 and 10.2). As the Rayleigh number rises, so do the values of turbulent viscosity. When the Rayleigh number goes from $Ra = 10^8$ to $Ra = 10^9$ in Fig.10.1, the values of turbulent viscosity along the horizontal axis at the mid-height of the tank completely increase. $Ra = 10^{10}$ and $Ra = 10^{11}$ in Fig.10.2, on the other hand, show that the values only rise near the axis for x less than 0.2 and stabilize elsewhere, canceling this variable.

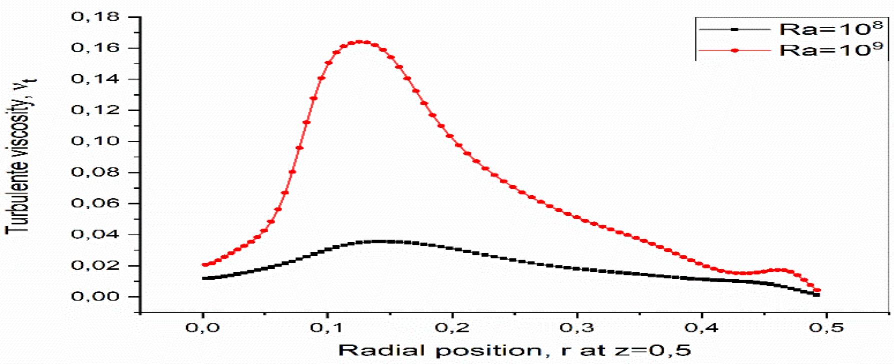

Fig.10.1 Turbulent viscosity at mid-height of the tank

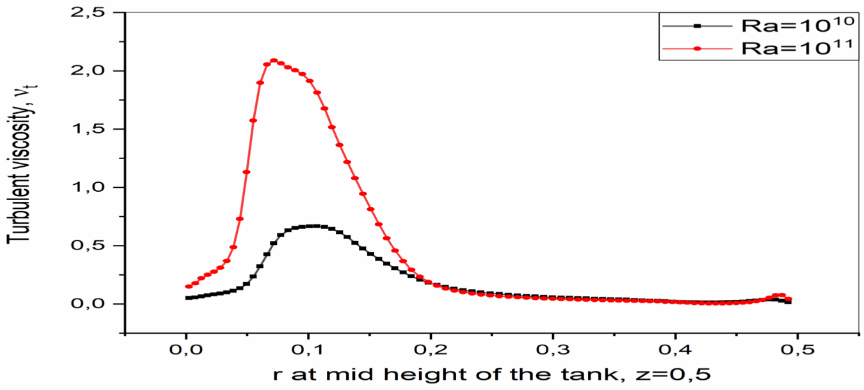

Fig.10.2 Turbulent viscosity at mid-height of the tank

Contours in the r-z plan are provided for turbulent viscosity to places where the turbulence generated is significant in the tank observed in Fig.11.1 and 11.2 in order to provide more information about this turbulent parameter. As you can see, the recirculation jets change direction near the central base, the first towards the sidewall, and the second towards the height. This is where the maximum turbulent viscosity is located. The friction between these two currents, which is inevitable, is undoubtedly responsible for this effect. These results also suggest that the turbulent viscosity exceeds the molecular viscosity if the Rayleigh number is greater than or equal to 10^{10}. For this Rayleigh number, it is approximately twice as large, while it is six times as large if that number is equal to 10^{11}.

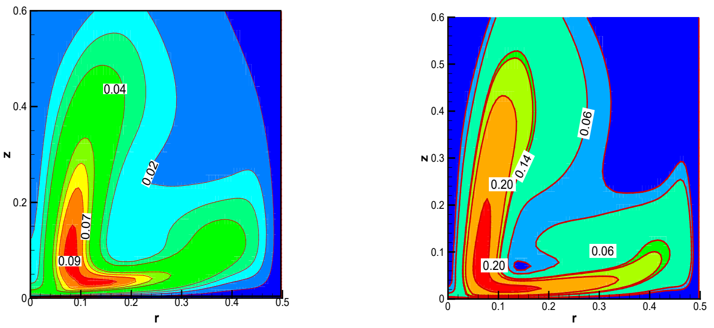

Fig.11.1 Turbulent viscosity contours in the tank for Ra=10^8 and Ra=10^9

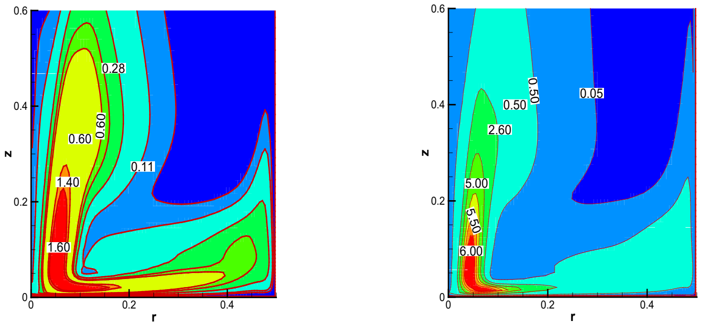

Fig.11.2 Turbulent viscosity contours in the tank for Ra=10^{10} and Ra=10^{11}

The findings of the present investigation into how the evaporative heat flux at the free surface changes for various Rayleigh numbers are shown in Fig.12. The study confirms that evaporation is non-uniform in turbulent flow, with the most evaporation occurring near the wall and the least at the center of the surface. Previous studies have shown that evaporation is non-uniform in laminar flow [15],[16], and [17]. Evaporation also increases close to the wall and slightly decreases at the surface's center as the Rayleigh number rises in the turbulent flow.

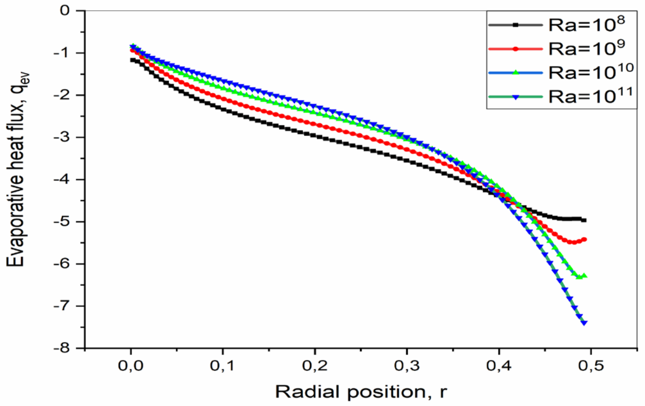

Fig.12 Variation of evaporative heat flux along radial position at the free surface with different Rayleigh Numbers.

3. Conclusions

When employing the standard k-epsilon model, previous numerical results in differentially heated square cavities indicated some variations from experimental results. In this work, a Reynolds low k-epsilon model (FLB model) is applied to improve numerical findings. In order to validate this actual code, we compare the results with those of experiments performed in a square cavity that was differently heated and contained air. Nusselt's experimental values along the hot and cold walls are in good agreement with numerical values. The turbulent kinetic energy (k) near the wall has a maximum value that is extremely close to 4.5, which is also quite close to the experimental result. Then, using the same model, the turbulent flow in a cylindrical LNG tank is quantitatively examined for Rayleigh numbers ranging from 10^8 to 10^{11}. The results are presented by axial and radial velocity fluctuations at the middle height of the tank, showing how the Rayleigh number affects the velocity profile and how the flow intensity rises with the number. Thermal and dynamic behavior are presented in two dimensions simultaneously in order to witness the second recirculation, which generates the jet upward toward the free surface.

The turbulent viscosities peak at 0.04 and 0.17, respectively, at the mid-height of the tank for Ra = 10^8 and Ra = 10^9. While in this position of the tank, the maximum viscosity varies from 0.7 to 2.2 for larger Rayleigh numbers. As a result, it is seen that a progressive rise in turbulent viscosity as Rayleigh numbers in the bottom tank rise, starting at Ra = 10^8. Because of this, it is confident that turbulence is starting to form in this part of the tank. Two things cause this: first, the fluid jet falls to the tank's central base; second, a small recirculation jet returns to the axis and creates an upward flow. The highest values of turbulent viscosity, which vary with Rayleigh number, are found in the center of the tank's bottom.

Finally, the variations in the evaporative heat flow are shown at the free surface according to the Rayleigh number.

Nomenclature				
a	Thermal diffusivity, m^2/s		r	Dimensionless horizontal coordinate
Ar	Aspect ratio, H/D		Ra	Rayleigh number, $\Delta T_0 H^3 Pr/\nu^2$
$C_{1\varepsilon}, C_{2\varepsilon}, C_{2\varepsilon}$	Coefficients in the equation of dissipation rate, ε		T	Dimensionless temperature
C_μ	Coefficient in the equation of viscosity		u	Dimensionless horizontal velocity
C_μ	Coefficient in the equation of viscosity		υ	Dimensionless vertical velocity
D	Diameter of the cavity, m		z	Dimensionless vertical coordinate
f_1	Correction factor for $C_{1\varepsilon}$		λ	Thermal conductivity, W/mK
f_2	Correction factor for $C_{2\varepsilon}$		β	Coefficient of thermal expansion
f_μ	Correction factor for C_μ		ΔT_0^*	Characteristic temperature difference, $q_l^* \lambda / H$
g	Acceleration of gravity, m/s^2		ε	Dimensionless rate of dissipation of turbulent kinetic energy
H	Height of the cavity, m		ν^*	Molecular kinematic viscosity, m^2/s
k	Dimensionless turbulent kinetic energy		ν_t^*	Turbulent kinematic viscosity, m^2/s
Nu_h	Nusselt number at the hot wall		ρ	Density, kg/m^3
Nu_c	Nusselt number at the cold wall		σ_k	Prandtl number for k
p	Dimensionless pressure		σ_ε	Prandtl number for ε
P_k	Dimensionless turbulent kinetic energy production term		σ_t	Prandtl number for T
Pr	Prandtl number, ν/a			

REFERENCES

[1] *F.Ampofo, T.G.Karayiannis*, Experimental benchmark data for turbulent natural convection in an air filled square cavity, Int. J. heat and Mass Transfer **46**, 2003, 3551-3572.

[2] *S. Vasic, K. Hanjalic*, Turbulent natural convection in a square cavity—benchmark computations, in: R.A.W.M. Henkes, C.J. Hoogendoorn (Eds.), Turbulent Natural Convection in Enclosures––A Computational and Experimental Benchmark Study, Editions Europeennes Thermique et Industrie, 1993, pp. 133–144.

[3] *S.H. Peng, L.Davidson,* Numerical investigation of turbulent buoyant cavity flow using LES, in: Third International Symposium on Turbulence, Int. J. Heat Mass Transfer, 2000, 1–8.

[4] *O. Khemis, R. Bessih, M. Ait Ali, M.X.Francois,* Measurement of heat transfers in cryogenic tank with several configurations, Appl. Therm. Eng **24,** 2004, 2233-2241.

[5] *D. Boukeffa, M. Boumaza, M.X. Francois, S. Pellerin,* Experimental and numerical analysis of heat losses in a liquid nitrogen cryostat, Appl. Therm. Eng **21**, 2001, 967-975.

[6] *T. Kanazawa, K. Kudo, A. Kurodo M. Tsui*, Experimental study on heat and fluid flow in LNG tank heated from the bottom and the sidewalls, Heat Transfer-Asian Res. 33, 2004, 417-330.

[7] *S.Bates, D.S. Morrison*, Modeling the behavior of stratified liquid natural gas in the storage tanks: a study of the rollover phenomenon, Int. J. Heat Mass Transfer 40, 1997, 1875-1984.

[8] *C.T. Pham, J. P. Petit*, Simultaneous heat and mass Transfers with or without evaporation in unsteady turbulent Natural convection and application to a liquefied natural gas Storage, 4th International Symposium on stratified flows Grenoble (F), , June 29- July 2, 1994.

[9] *Y. Li. C. Wang, R. Wang*, Study on effect of liquid level on the heat leak into vertical cryogenic vessels, Cryogenics 50, 2010, 367-372.

[10] *Hubert, A., Dembele, S., Denissenko, P. & Wen, J*, Predicting Liquefied Natural Gas (LNG) rollovers using Computational Fluid Dynamics. Journal of Loss Prevention in the Process Industries, 62, 103922.

[11] *S. Roh, G. Son.* NumericalStudy of convection in a liquefied natural gas tank, J. Mech. Sci. and Tech **26**, 2012, 3133-3140.

[12] *Q.S. Chen, J. Wegryzyn, V. Orasad,,* Analysis of temperature and pressure changes in liquefied natural gas (LNG) cryogenic tanks, cryogenics **44**, 2004,701-709.

[13] *Haddar, M., Hammami, M. & Baccar, M*, Numerical parametric study of a cooling system for an LNG storage tank. Oil & Gas Science and Technology–Revue d'IFP Energies nouvelles, **74**, 2019, 21.

[14] *W.M.F. Hasan, A.M. Zheng. I.A. Karimi,* Minimizing boil-off losses in liquefied natural gas transportation, Ind. Eng. Chem. **48,** 2009, 9571-9580.

[15] *M.S. Khelifi Touhami, A. Benbrik, D. Lemonnier, D. Blay,* Laminar natural convection flow in a cylindrical cavity application to the storage of LNG.J. Pet. Sci. Eng, **71**, 2010, pp. 126- 132.

[16] *Kozhevnikov, D. A. & Sheremet, M. A*, Natural convection with evaporation in a vertical cylindrical cavity under the effect of temperature-dependent surface tension. Continuum Mechanics and Thermodynamics, **30**, 2018, 83-94.

[17] *K. Rachedi, H. Ragueb, M. Boussaid,,* Numerical investigation of surface evaporation and thermo capillarity effects on natural convection within a contained fluid in cryogenic tank, J. Pet. Sci. Eng, **volume 214**, 2022, 110533.

[18] *B.E. Launder and D.B. Spalding,* The numerical computation of turbulent flows, computer Methods in Applied Mechanics and Engineering, **vol. 3**, 1974, pp. 269-289.

[19*] S.Fan, B. Lakshminarayana and M.Barnett*, Low-Reynolds-number k-epsilon model for unsteady turbulent boundary layer flows, AIAA JOURNAL **vol. 31**, No. 10, October 1993, 1777-1784.

[20] *H.T. Hashemi and H.R. Wesson,* Cut LNG storage costs, Hydrocarbon Processing, August 1971, pp. 246-249.

[21] *Versteeg and W. Malalasekera,* An introduction to computational fluid dynamics the finite volume method Edinburgh Gate Harlow Essex CM 2JE England, 1995.

[22] Compaq visual Fortran software